


Anion Dependent Redox Changes in Iron Bis-terdentate Nitroxide {NNO} Chelates

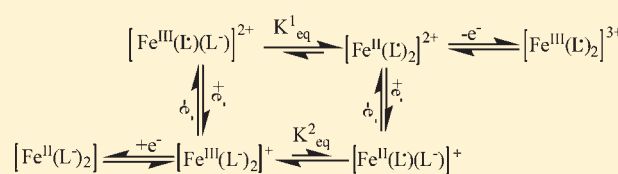
Ian A. Gass,[†] Christopher J. Gartshore,[†] David W. Lupton,[†] Boujemaa Moubaraki,[†] Ayman Nafady,[†] Alan M. Bond,[†] John F. Boas,[‡] John D. Cashion,[‡] Carsten Milsmann,[§] Karl Wieghardt,^{*,§} and Keith S. Murray^{*,†}

[†]School of Chemistry and [‡]School of Physics, Monash University, Clayton, Victoria 3800, Australia

[§]Max-Planck Institute of Bioinorganic Chemistry, Stiftstrasse 34-36, D-45470 Mülheim an der Ruhr, Germany

 Supporting Information

ABSTRACT: The reaction of $[\text{Fe}^{\text{II}}(\text{BF}_4)_2] \cdot 6\text{H}_2\text{O}$ with the nitroxide radical, 4,4-dimethyl-2,2-di(2-pyridyl) oxazolidine-*N*-oxide (L^\bullet), produces the mononuclear transition metal complex $[\text{Fe}^{\text{II}}(\text{L}^\bullet)_2](\text{BF}_4)_2$ (**1**) which has been investigated using temperature dependent susceptibility, Mössbauer spectroscopy, electrochemistry, density functional theory (DFT) calculations, and X-ray structure analysis. Single crystal X-ray diffraction analysis and Mössbauer measurements reveal an octahedral low spin Fe^{2+} environment where the pyridyl donors from L^\bullet coordinate equatorially while the oxygen containing the radical from L^\bullet coordinates axially forming a linear $\text{O}^\bullet \cdot \text{Fe}(\text{II}) \cdot \text{O}^\bullet$ arrangement. Magnetic susceptibility measurements show a strong radical–radical intramolecular antiferromagnetic interaction mediated by the diamagnetic Fe^{2+} center. This is supported by DFT calculations which show a mutual spatial overlap of 0.24 and a spin density population analysis which highlights the antiparallel spin alignment between the two ligands. Similarly the monocationic complex $[\text{Fe}^{\text{III}}(\text{L}^-)_2](\text{BPh}_4) \cdot 0.5\text{H}_2\text{O}$ (**2**) has been fully characterized with Fe–ligand and N–O bond length changes in the X-ray structure analysis, magnetic measurements revealing a Curie-like $S = 1/2$ ground state, electron paramagnetic resonance (EPR) spectra, DFT calculations, and electrochemistry measurements all consistent with assignment of Fe in the (III) state and both ligands in the L^- form. **2** is formed by a rare, reductively induced oxidation of the Fe center, and all physical data are self-consistent. The electrochemical studies were undertaken for both **1** and **2**, thus allowing common Fe–ligand redox intermediates to be identified and the results interpreted in terms of square reaction schemes.



INTRODUCTION

Iron complexes of chelating organic radical ligands, such as those of the diimine type, have recently been shown to be very important in olefin polymerization catalysis, when the Fe center has a vacant coordination site.¹ From the general perspective of redox-active (non-innocent) ligands such as N,N; N,S; S,S and other donors, detailed studies of the synthesis, structure, magnetism, spectra, electrochemistry, and density functional theory (DFT) calculations of their iron (and other d-block ions) chelates, in varying coordination geometries, have yielded valuable information on their electronic structure, electron transfer properties, reactivity, and spin-exchange coupling between metal and ligand, or ligand–ligand spins.² Such data are important, also, in regard to gaining a full understanding of metalloenzymes and their active sites that involve radicals such as tyrosyl, coordinated, for example, to Cu(II).^{1,3}

In the area of molecule-based magnetism, the use of the tetracyanoethylene radical anion in the charge transfer complex $[\text{Fe}(\eta^5\text{-C}_5\text{Me}_5)_2]^+[\text{TCNE}]^{\bullet -}$ led to the first example of a molecular based ferromagnet.⁴ This idea of using such an organic spin carrier in conjunction with paramagnetic metal ions as building blocks in preparing novel molecular magnetic materials was labeled the “metal-radical approach” and was developed by

Gatteschi and co-workers with the use of nitroxide radicals.⁵ Nitroxides are well-known stable organic radicals⁶ and have been widely used initially as spin probes⁷ and pure organic ferromagnets.⁸ Nitroxides can be considered as weak Lewis bases and so are not expected to coordinate directly to metal centers unless the Lewis acidity of the metal is increased by electron-withdrawing groups such as hexafluoroacetylacetonato (hfac^-). Indeed, ferrimagnetic ordering in $\text{Mn}^{\text{II}}(\text{hfac})_2\text{L}$ complexes using a *tert*-butyl-nitroxide triradical has been observed,⁹ and the single chain magnet $[\text{Co}^{\text{II}}(\text{hfac})_2(\text{rad})]$ shows magnetic relaxation of spin flips.¹⁰ Alternative strategies to coordinate weakly basic nitroxides to metal centers involves incorporation of the radical in “conventional” strongly ligating systems such as pyridine,¹¹ pyrazine,¹² 2,2'-bipyridine,¹³ and imidazole.¹⁴ Here the coordinating ligands can orient the radical portion in close proximity (e.g., via chelation) to the metal leading to exchange between the radical spin and the paired electrons on the metal center. Such exchange is highly dependent on the relevant orientation of the magnetic orbitals where the sign of the coupling of a nitroxide bound to a metal ion is ferromagnetic when the orbitals

Received: December 30, 2010

Published: March 08, 2011

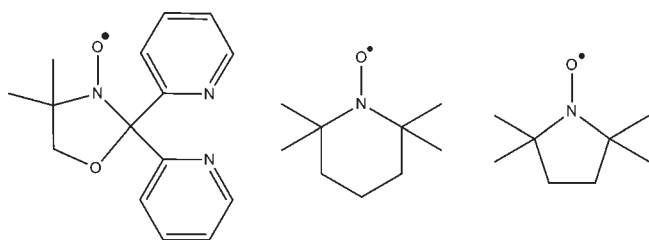


Figure 1. Structural formulas of 4-dimethyl-2,2-di(2-pyridyl) oxazolidine *N*-oxide (L^*) (left), Tempo (middle), and Proxyl (right) as discussed in the text.

containing the radical and the unpaired electrons on the metal ion are orthogonal to each other and antiferromagnetic when there is significant overlap.⁵

Surprisingly, the vast majority of metal nitroxide complexes contain metal ions other than Fe^{2+} and to the best of our knowledge there are only three papers involving Fe^{2+} and nitroxide radicals.^{13,15,16} Here we report on the synthesis of $[Fe^{II}(L^*)_2](BF_4)_2$, **1**, where the Fe^{2+} ion is in the low spin state and (close to) diamagnetic, thus offering a rare model complex to study the effect of the radical–radical interaction through a diamagnetic metal ion other than Zn^{2+} . The ligand used for the preparation of $[Fe^{II}(L^*)_2](BF_4)_2$ is the nitroxide radical, 4,4-dimethyl-2,2-di(2-pyridyl) oxazolidine-*N*-oxide (L^*) used previously to create Cu^{II} and Zn^{II} complexes (Figure 1).¹⁷ Our interest in Fe^{II} complexes using this ligand initially stemmed from an attempt to investigate the effect of radical- Fe^{II} exchange on the potential of Fe^{II} to undergo a thermally induced $S = 0$ to $S = 2$ spin transition¹⁸ in such an N_4O_2 environment¹⁹ in a similar vein to the $S = 1/2$ to $S = 3/2$ spin-crossover and exchange seen, simultaneously, in a radical $Fe^{III}(S_4O)$ complex.^{18c} It turned out, however, that there is no spin crossover in **1**. Interestingly, when the anion was swapped to BPh_4^- , the reaction in air, in methanol, yielded the crystalline monocationic product $[Fe^{III}(L^*)_2](BPh_4) \cdot 0.5H_2O$ (**2**), the physical and structural properties of which showed it to have the + (III) oxidation state on Fe and the reduced form of both ligands. It is formed by a rare, but not unknown, reductively induced oxidation of the central iron.

EXPERIMENTAL SECTION

General Procedures. All reagents and solvents were of reagent grade and used as received. Microanalyses were performed by the Campbell Microanalytical Laboratory, Chemistry Department, University of Otago, Dunedin, New Zealand.

Di(pyridin-2-yl)methanone. The title compound was prepared using a modification to the conditions reported by Ito et al.¹⁷ *n*-Butyl lithium (5.3 mL of a 1.2 M solution in hexane, 6.33 mmol) was added, dropwise, to a stirred solution of 2-bromopyridine (0.6 mL, 6.33 mmol) in tetrahydrofuran (THF, 10 mL) at -78 °C. After stirring at this temperature for 1 h, ethyl chloroformate (0.3 mL, 2.85 mmol) was added, and the reaction was allowed to warm to room temperature and stirred for an additional 12 h. After this time the reaction was quenched with water (5 mL), and the aqueous layer was extracted with dichloromethane (3×10 mL). The combined organic was washed with $NaHCO_3$ (15 mL of a sat. aq. solution), brine (10 mL), and dried over $MgSO_4$. The solution was then filtered and concentrated in vacuo to yield a brown oil. Purification via flash column chromatography (SiO_2 ; EtOAc) yielded an orange solid (0.51 g, 97%). R_f 0.35 (EtOAc) 1H NMR (400 MHz): 8.75 (d, $J = 4.8, 1.2$ 2H), 8.09 (d, $J = 7.6, 1.2$ 2H),

7.89 (t, $dJ = 7.6, 1.2$ 2H), 7.48 (d, $d,dJ = 7.6, 4.8, 1.2$ 2H). ^{13}C NMR (100 MHz): 192.45, 153.76, 148.66, 136.29, 125.96, 124.75. MS (ESI⁺, MeOH): m/z 185.1 $[M + H]^+$; $C_{11}H_9N_2O$ requires 185.2

4,4-Dimethyl-2,2-di(pyridin-2-yl)oxazolidine. The title compound was prepared using the procedure of Ito et al.¹⁷ Purification was achieved by flash column chromatography (SiO_2 , 1:1 Hexane/EtOAc) to afford the title compound as a pale orange solid (673 mg, 98%). R_f 0.05 (Hex/EtOAc 1:1). Mp $72-73$ °C 1H NMR (400 MHz): 8.52 (d, $J = 4.8, 1.2$ 2H), 7.72 (d, $tJ = 8.0, 1.2$ 2H), 7.60 (t, $dJ = 8.0, 1.2$ 2H), 7.11, (d, $d,dJ = 8.0, 4.8, 1.2$ 2H), 4.23 (bs, 1H), 3.65 (s, 2H), 1.18 (s, 6H); ^{13}C NMR (100 MHz): 162.52, 148.66, 136.51, 122.47, 121.40, 99.10, 78.15, 59.84, 26.81 ν_{max} (KBr): 2977, 2862, 1586, 1466, 1428, 1255, 1040, 779; MS (ESI⁺, MeOH): m/z 256.2 $[M + H]^+$; $C_{15}H_{17}N_3O$ requires 256.3.

4,4-Dimethyl-2,2-di(pyridin-2-yl)oxazolidine N-oxide (L).* The title compound was prepared using the procedure of Ito et al.¹⁷ Purification was achieved by flash column chromatography (SiO_2 , 95:5 EtOAc/MeOH) and afforded the title compound as an orange solid (90 mg, 85%). R_f 0.15 (EtOAc/MeOH 95:5). Mp $91-94$ °C ν_{max} (KBr): 3380, 2982, 1696, 1588, 1434, 908 MS (ESI⁺, MeOH): m/z 293.1 $[M + Na]^+$; $C_{15}H_{16}N_3NaO_2$ requires 293.3.

$[Fe^{II}(L^*)_2](BF_4)_2$ (**1**). Twenty-five milligrams (0.0925 mmol) of 4,4-dimethyl-2,2-di(2-pyridyl) oxazolidine *N*-oxide (L^*) and 15.6 mg (0.04625 mmol) of $Fe^{II}(BF_4)_2 \cdot 6H_2O$ were dissolved in 10 mL of acetonitrile. After 5 min of stirring, the resultant emerald green solution was filtered and diffused with Et_2O to produce X-ray quality crystals, after 3 days, in 56% yield (19.9 mg). Anal. Calcd (%) for **1**, $C_{30}H_{32}N_6O_4B_2F_8Fe$: C, 46.8; H, 4.2; N, 10.9. Found: C, 46.4; H, 4.1; N, 10.7. IR (ATR cm^{-1}): 3095w, 1601w, 1571 m, 1464 m, 1444 m, 1392w, 1371w, 1282 m, 1236w, 1172 m, 1036s, 788 m, 772s, 771w, 659w.

$[Fe^{III}(L^*)_2](BPh_4) \cdot 0.5H_2O$ (**2**). Twenty-five milligrams (0.0925 mmol) of 4,4-dimethyl-2,2-di(2-pyridyl) oxazolidine-*N*-oxide (L^*), 12.9 mg (0.04625 mmol) of $Fe^{III}(SO_4) \cdot 7H_2O$, and 31.6 mg (0.0925 mmol) of $Na(BPh_4)$ were dissolved in 10 mL of methanol. After 60 min stirring, the resultant green precipitate was dissolved in CH_2Cl_2 , filtered, and diffused with Et_2O to produce X-ray quality crystals of **2** after 1 day. Yield 35 mg (40.9%). Anal. Calcd (%) for **2**, $C_{54}H_{52}N_6O_4BFe \cdot 0.5H_2O$: C, 70.1; H, 5.8; N, 9.1. Found: C, 70.2; H, 5.7; N, 9.1. IR (ATR cm^{-1}): 3057 m, 3035 m, 2983 m, 2970 m, 2941w, 2886w, 1605 m, 1579 m, 1462s, 1429s, 1362 m, 1292s, 1273 m, 1224 m, 1189 m, 1142 m, 1075 m, 1029w, 1010w, 988 m, 955 m, 901w, 848w, 764s, 732s, 701s, 682s, 669 m 651s, 606w.

Magnetic Susceptibility Measurements. Variable-temperature, solid state direct current (dc) magnetic susceptibility data down to 5 K were collected with an applied field of 0.5 T on a Quantum Design MPMS 7T SQUID magnetometer calibrated by use of a standard palladium sample (Quantum Design) of accurately known magnetization or by use of magnetochemical calibrants such as $CuSO_4 \cdot 5H_2O$. Microcrystalline samples were dispersed in Vaseline to avoid torquing of the crystallites. The sample mulls were contained in a calibrated capsule held at the center of a drinking straw that was fixed at the end of the sample rod.

X-ray Crystallography. X-ray crystallographic measurements were performed at 123(2) K using a Bruker Smart Apex X8 diffractometer with $Mo K\alpha$ radiation. Single crystals were mounted on a glass fiber using oil. The data collection and integration were performed within SMART and SAINT+ software programs, and corrected for absorption using the Bruker SADABS program. Crystallographic data and refinement parameters for **1** and **2**, given in Table 1, were solved by direct methods (SHELXS-97), and refined (SHELXL-97) by full least-squares on all F^2 data.²⁰ In both cases, the asymmetric unit contains two nonidentical halves of the monomer with the inversion center located on the iron ions of each identifiable monomer half. There are two tetrafluoroborate anions per monomer for **1** and one tetraphenylborate

Table 1. Crystallographic Data for **1** and **2**

	1	2
formula	C ₃₀ H ₃₂ N ₆ O ₄ B ₂ F ₈ Fe	C ₅₄ H ₅₃ N ₆ O _{4.5} BFe
<i>M_r</i>	770.09	924.69
crystal system	triclinic	triclinic
space group	<i>P</i> $\bar{1}$	<i>P</i> $\bar{1}$
<i>a</i> /Å	9.5140(7)	8.4571(7)
<i>b</i> /Å	13.0947(10)	12.7587(9)
<i>c</i> /Å	13.2183(10)	23.0359(16)
α /deg	89.994(2)	74.257(2)
β /deg	86.119(3)	80.636(2)
γ /deg	75.890(2)	71.623(2)
<i>V</i> /Å ³	1593.2	2262.3(3)
<i>T</i> /K	123(2)	123(2)
<i>Z</i>	2	2
$\rho_{\text{calc}}/\text{g cm}^{-3}$	1.605	1.356
λ /Å	0.71073	0.71073
ind. reflns	7162	10234
reflns with <i>I</i> > 2σ(<i>I</i>)	4970	8301
parameters	467	611
restraints	0	6
final <i>R</i> ₁ , <i>wR</i> ₂ [<i>I</i> > 2σ(<i>I</i>)]	0.0541, 0.1192	0.0668, 0.1234
<i>R</i> ₁ , <i>wR</i> ₂ all data	0.0878, 0.1346	0.0855, 0.1315
goodness of fit	1.043	1.118
largest residuals/e Å ⁻³	0.660, -0.527	0.930, -0.502

for **2**. The solvate water in **2** is half occupied and restrained with ISOR with no hydrogen atom placement. All other non-hydrogen atoms in **1** and **2** are refined anisotropically and all hydrogen atoms are placed in calculated positions. CCDC numbers are 803710 (**1**) and 803711 (**2**). Full crystallographic data for **1** to **2** are available on request from the Cambridge Crystallographic Data Centre, 12 Union Road, Cambridge CB2 1EZ, U.K. (<http://www.ccdc.cam.ac.uk/>).

Mössbauer Spectroscopy. Mössbauer spectra were measured by use of a standard electromechanical transducer operating in a symmetrical constant acceleration mode. A conventional bath cryostat was employed for temperature control with the sample maintained in exchange gas. Spectra were collected with a 1024-channel multianalyzer. Velocity calibration was made with respect to α -iron foil and isomer shifts are quoted with respect to α -iron at room temperature. Spectra were fitted using Lorentzian and Voigtian lineshapes.

Quantum-Chemical Calculations. All DFT calculations were performed using the ORCA program package.²¹ The geometry optimizations of the complexes were carried out at the BP86^{22–24} level of DFT. Single-point calculations on the optimized geometries were carried out using the B3LYP^{25,26} functional. This hybrid functional often gives better results for transition metal compounds than pure gradient-corrected functionals, especially with regard to metal–ligand covalency. The def2-TZVP(-f) (Fe, N, and O) and def2-SV(P) (C and H) basis sets²⁷ were applied in combination with the auxiliary basis sets def2-TZVP/J (Fe, N, and O) and def2-SVP/J (C and H).^{28–30} The RI^{28–30} and RIJCOSX³¹ approximations were used to accelerate the calculations. Throughout this paper we describe our computational results by using the broken-symmetry (BS) approach developed by Ginsberg³² and Noodleman et al.³³ Because several broken symmetry solutions to the spin-unrestricted Kohn–Sham equations may be obtained, the general notation BS(*m,n*)³⁴ has been adopted, where *m* (*n*) denotes the number of spin-up (spin-down) electrons at the two interacting fragments. Canonical and corresponding orbitals, as well as spin density plots were generated with the program Molekel.³⁵ Nonrelativistic single-point

calculations on the optimized geometry were carried out to predict Mössbauer spectral parameters (isomer shifts and quadrupole splittings).³⁶ These calculations employed the CP(PPP)³⁷ basis set for iron. The Mössbauer isomer shifts were calculated from the computed electron densities at the iron centers as previously described.³⁶

Electrochemistry. Voltammetric measurements were undertaken in acetonitrile (0.1 M [Bu₄N](PF₆)) at 293 ± 2 K under a flow of nitrogen gas or inside a glovebox using a BAS100B computer-controlled electrochemical workstation and a standard three-electrode cell. Glassy carbon (1.5 mm diameter, Cypress) macro-electrode and platinum (10 μm diameter, custom-made) microelectrode were used as the working electrode, whereas a platinum mesh and Ag/AgCl electrode, separated from the test solution by a salt bridge containing CH₃CN (0.1 M [Bu₄N][PF₆]), was used as the counter and reference electrodes, respectively. The procedures employed for polishing the working electrode are described elsewhere.³⁸ All potentials given in this paper are referred to the ferrocene/ferrocenium ([FeCp₂]^{0/+}) reference couple. Mechanistic aspects of the voltammetric processes were investigated by applying the appropriate diagnostic criteria.³⁹

Electron Paramagnetic Resonance (EPR) Spectra. X-band (ca. 9.4 GHz) EPR spectra were recorded with a Bruker ESP380E CW/FT spectrometer using the standard rectangular TE₁₀₂ rectangular cavity. Sample temperatures from room temperature (293 K) to about 110 K were obtained with a Bruker VT 4111 temperature controller and its associated nitrogen gas flow insert and spectra at 77 K using a quartz finger dewar. Spectra in the temperature range 100 K down to 2.5 K were obtained using a Bruker ER4118 dielectric resonator inserted in an Oxford Instruments CF 935 helium cryostat. Temperatures below 100 K were calibrated against a germanium thermometer using a carbon resistor as a transfer standard. Microwave frequencies were measured with an EIP Microwave 548A frequency counter, and the *g*-factors were determined by reference to the F⁺ line in CaO (*g* = 2.0001 ± 0.0001).⁴⁰ Uncertainties in the *g*-values reported below are estimated as being ±0.0005. Spectrum simulations were performed using the Bruker XSophe-Sophe-XeprView computer simulation software suite.⁴¹ Spectral intensities were computed by double integration of the first derivative spectrum obtained experimentally by using the integration routine in the Bruker WINEPR suite. The estimate of spin concentration was made by comparison with CuSO₄·5H₂O.

RESULTS AND DISCUSSION

Synthesis and Structure. [Fe^{II}(L[•])₂][BF₄]₂, **1**, was isolated, simply, via the reaction of 4,4-dimethyl-2,2-di(2-pyridyl) oxazolidine-*N*-oxide (L[•]) with [Fe^{II}(BF₄)₂]·6H₂O in a 2:1 ratio in MeCN. The resulting emerald green solution was diffused with Et₂O to produce X-ray quality green crystals. The monocationic complex [Fe^{III}(L⁻)₂](BPh₄)·0.5H₂O, **2**, was isolated via the reaction of L[•] with Fe^{II}(SO₄)·7H₂O and Na(BPh₄) in a 2:1:2 ratio in MeOH, in air, the resultant precipitate being dissolved in CH₂Cl₂ and diffused with Et₂O to produce X-ray quality dichroic crystals. The synthesis of **2** is assumed to involve formation of **1** followed by rapid reduction of the ligand and oxidation of [BPh₄]⁻ anion via an internal electron transfer reaction.

Complexes **1** and **2** both crystallize in the triclinic space group *P* $\bar{1}$, at 123 K, with the asymmetric unit of **1** containing two distinct cation [Fe^{II}(L[•])₂]²⁺ halves and two tetrafluoroborate anions while **2** contains two distinct [Fe^{III}(L⁻)₂]⁺ halves, one tetraphenylborate anion and half a solvate water. The inversion centers in **1** and **2** lie on the Fe²⁺ ions generating two unique [Fe^{II}(L[•])₂]²⁺ cations in **1** and two unique [Fe^{III}(L⁻)₂]⁺ cations in **2**, the two cations within each complex differing only in a slight variation of bond lengths and angles (Figure 2). The cations in **1**

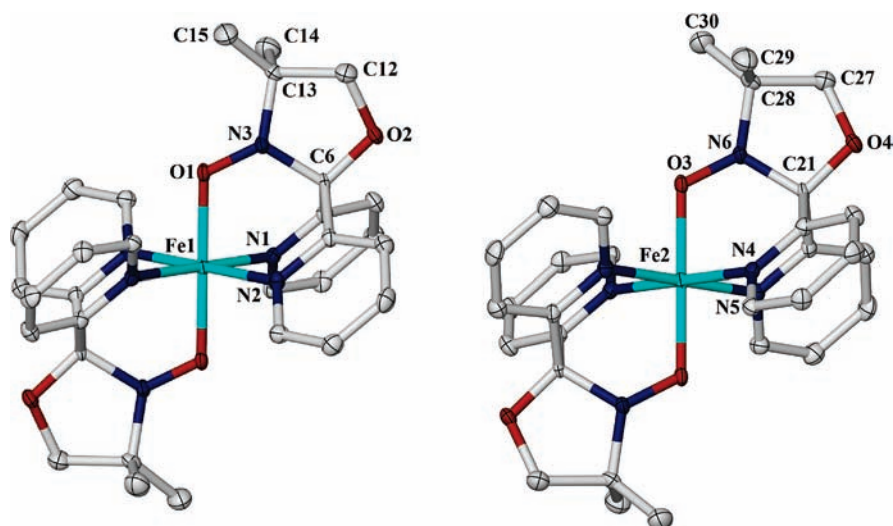


Figure 2. Molecular structure of the two crystallographically independent cations in **1** and **2**. Hydrogen atoms and anions omitted for clarity. Oxygen, red; nitrogen, dark blue; iron(II), turquoise.

Table 2. Selected Bond Lengths (Å) and Angles (deg) for **1** and **2** at 123 K

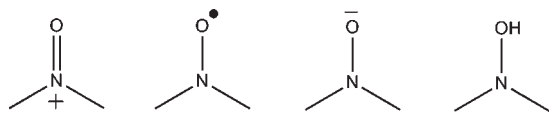
	1		2		
	[Fe(1)(L ⁺) ₂] ²⁺	[Fe(1)(L ⁻) ₂] ⁺	[Fe(2)(L ⁺) ₂] ²⁺	[Fe(2)(L ⁻) ₂] ⁺	
Fe(1)–O(1)	1.876(2)	1.856(2)	Fe(2)–O(3)	1.884(2)	1.859(2)
Fe(1)–N(1)	1.973(2)	1.964(2)	Fe(2)–N(4)	1.962(2)	1.957(2)
Fe(1)–N(2)	1.982(2)	1.996(2)	Fe(2)–N(5)	1.989(2)	1.982(2)
O(1)–N(3)	1.317(3)	1.411(3)	O(3)–N(6)	1.314(3)	1.412(3)
N(3)–C(6)	1.467(4)	1.477(4)	N(6)–C(21)	1.473(4)	1.477(4)
N(3)–C(13)	1.470(4)	1.483(4)	N(6)–C(28)	1.476(3)	1.494(4)
C(6)–O(2)	1.399(4)	1.405(3)	C(21)–O(4)	1.394(3)	1.408(3)
O(2)–C(12)	1.440(4)	1.458(4)	O(4)–C(27)	1.453(4)	1.449(4)
C(12)–C(13)	1.536(5)	1.529(4)	C(27)–C(28)	1.520(4)	1.533(4)
C(13)–C(14)	1.516(5)	1.528(4)	C(28)–C(29)	1.536(5)	1.528(4)
C(13)–C(15)	1.514(5)	1.518(4)	C(28)–C(30)	1.508(4)	1.529(4)
Fe(1)–O(1)–N(3)	117.58(16)	115.53(16)	Fe(2)–O(3)–N(6)	117.50(16)	115.92(16)

1 and **2** are structurally similar but differ in a few significant bond lengths and angles. In **1** and **2** each Fe²⁺ (or Fe^{III}) ion is in a distorted octahedral geometry (cis, 86.64(10)–93.36(10)°, 86.41(10)–92.27(9)°; trans, all 180°; octahedral distortion parameter⁴² $\Sigma = 22.56^\circ, 26.32^\circ$ for Fe1 and Fe2 in **1**, respectively, and cis, 85.62(10)–94.38(10)°, 85.66(9)–94.34(9)°; trans, all 180°; octahedral distortion parameter⁴² $\Sigma = 42^\circ, 38.68^\circ$ for Fe1 and Fe2 in **2**, respectively). Fe–N distances in **1** are 1.973(2) and 1.982(2) Å for Fe1 and 1.962(2) and 1.989(2) Å for Fe2 while in **2** they are 1.964(2) and 1.996(2) Å for Fe1 and 1.957(2) and 1.982(2) Å for Fe2. These are shorter than for the [Cu^{II}(L⁺)₂](CF₃SO₃)₂ and [Zn^{II}(L⁺)₂](CF₃SO₃)₂ analogues in which Cu–N = 2.01 Å(av.) and Zn–N = 2.12 Å(av.). The Fe–O distances are short; 1.876(2) and 1.884(2) Å, for Fe1 and Fe2 in **1** and 1.856(2) and 1.859(2) Å for Fe1 and Fe2 in **2**, respectively (Table 2). The nitroxide N–O bond lengths are 1.317(3) and 1.314(3) Å in **1** and 1.411(3) and 1.412(3) Å in **2** for the cations associated with Fe1 and Fe2, respectively. The deviation of the nitroxide nitrogens N3 and N6 from the planes

defined by O1–C6–C13 and O3–C21–C28, respectively, are larger in **2** than in **1** which is presumably due to accommodation of the longer nitroxide N–O bond length. In both **1** and **2** the ligand L acts as a tridentate chelator with the two pyridyl donors coordinating equatorially and the oxygen coordinating axially, thus completing the coordination sphere of the Fe ions. In **1**, two tetrafluoroborate anions, per cation, are present in the lattice with no solvent or any significant intermolecular interaction being present (the shortest O_{NO}–O_{NO} intermolecular distance between neighboring nitroxide groups is 7.172 Å). In **2**, one tetraphenylborate anion and half a water molecule, per cation, is present in the lattice with again no significant intermolecular interactions present. The shortest O_{NO}–O_{NO} intermolecular distance between neighboring nitroxide groups is 5.269 Å.

The short Fe–O distances in **1** and **2** contrasts with the analogous, axially elongated [Cu^{II}(L⁺)₂](CF₃SO₃)₂ complex, Cu–O = 2.333 Å(av.) and the [Zn^{II}(L⁺)₂](CF₃SO₃)₂ complex with Zn–O = 2.163 Å(av.).¹⁷ The only crystallographic data available on a ferrous radical complex is for [Fe₃Cl₂(TMRASQ)₄

Scheme 1. Sketch of the Nitrosonium Cation (left), Neutral Nitroxide Radical, Hydroxylamino Anion, and the Hydroxylamine Group (right)



(HTMRA)₂] · C₅H₁₂ (TMRASQ = 4,4,5,5-tetramethyl-2,3-dihydroxy-2-cyclopenten-1-one; HTMRA = the semiquinone form) in which the high spin ferrous Fe–O bond lengths are 2.116(2) and 2.137(2) Å.⁴³ The Fe–O bond lengths in **1** and **2** are shorter than typical low spin ferrous Fe–O bond lengths found in non radical ligand systems that generally range from 1.930(1) to 1.967(3) Å,¹⁹ thus suggesting that a strong interaction between the nitroxide N–O oxygen and the low spin Fe(II), or Fe(III), plays a part in the shortening of the Fe–O bond in **1** and **2**. A compressed octahedral geometry is therefore realized.

Assignment of the redox states of the ligands in complexes **1** and **2** is necessary in terms of the neutral radical, L[•], or corresponding reduced forms, L[−] (Scheme 1). The nitroxide N–O bond lengths are particularly useful in identifying possible redox states. Thus, free ligand radicals such as NITR, Tempo, and Proxyl have nitroxide N–O bond lengths of 1.28 Å, 1.28 Å and 1.27 Å, respectively,⁶ while coordination of NITR in a series of [Mn(hfac)₂NITR] complexes shows a lengthening of the coordinated nitroxide N–O bond length to the range 1.289 Å to 1.322 Å and stems from a nonzero overlap between the metal and radical orbitals.⁶ The corresponding nitrosonium cation found in [NITPh](ClO₄)⁴⁴ has an average N–O bond length of 1.225(4) Å consistent with values expected for an N=O bond while N–O bond lengths of 1.333(4), 1.367(3), and 1.342(4) Å are found in a series of Fe²⁺ complexes involving the reduced form of the IM2py radical.⁴⁵ A more fitting comparison with L would be with transition metal complexes of the Tempo and Proxyl radicals (See Figure 1) which have two sp³ carbons adjacent to the nitroxide N–O in a similar way to L. For both Tempo and Proxyl 3d transition metal complexes the N–O bond length in the coordinated radical species is in the range 1.261(12)–1.300(3) Å^{46–52} while for Tempo the equivalent coordinated hydroxylamino anion or hydroxylamine groups have N–O bond lengths in the range 1.379(5)–1.413(3) Å.^{53–55} A recent paper on Cu(II) *t*-butyl-2-pyridyl-nitroxide (2pyNO) bis-chelates (with 5-membered CuONCN(py) rings) has presented similar arguments concerning N–O bond lengths and the redox state of the bidentate pyridyl-nitroxide.^{11c} The N–O bond lengths from the two cations in complex **1** of 1.317(3) and 1.314(3) Å suggest that the ligand is in the neutral coordinated radical form (L[•]) with bond order 1.5. This is also the case in the [Cu^{II}(L[•])₂](CF₃SO₃)₂ and [Zn^{II}(L[•])₂](CF₃SO₃)₂ analogues, these showing N–O lengths of 1.272(1) and 1.282(1) Å, respectively.¹⁷ The Cu–O–N and Zn–O–N angles (110.3° and 114.2°) are lower than the Fe–O–N angle, 117.5°, in **1**. Support for assignment of L[•] in complex **1** comes not only from the bond lengths, just discussed, but also from the interpretation of electrochemistry and DFT calculations (vide infra).

In complex **2** the N–O bond lengths from the two monocations of 1.411(3) and 1.412(3) are indicative of a bond order of 1 with both ligands being in the reduced L[−] form. Together with the slightly shorter Fe–ligand distances in **2** compared to **1**, this is indicative of the metal oxidation state being Fe(III) and low spin. Susceptibility, Mössbauer effect, and EPR spectral

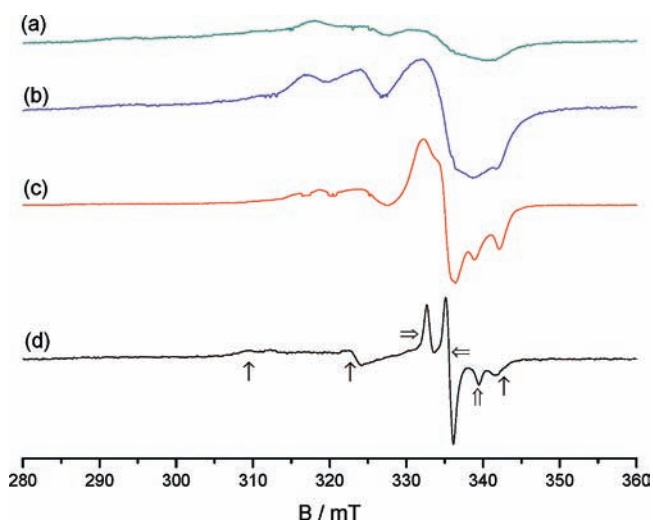


Figure 3. EPR spectra of **1**. Polycrystalline powder: (a) 300 K, (b) 180 K, (c) 110 K. Spectrometer settings: microwave frequency 9.434 GHz, receiver gain 1.0×10^5 (300 and 180 K), 2.5×10^4 (110 K), 100 kHz modulation amplitude 0.5 mT, microwave power 5.26 mW. (d) Frozen solution 5 mM in MeCN at 120 K: microwave frequency 9.427 GHz, receiver gain 1.0×10^5 , 100 kHz modulation amplitude 0.2 mT, microwave power 2.09 mW. All spectra recorded with magnetic field scan 100 mT/84 s, time constant 81.9 ms. In the frozen solution spectrum the single arrows indicate the peaks ascribed to **2** (see Figure 4); the double arrows those ascribed to the nitroxide radical.

measurements, and DFT calculations (vide infra) confirm the low spin d^5 formulation [Fe^{III}(L[−])₂]⁺ for **2**.

EPR Spectroscopy. [Fe^{II}(L[•])₂](BF₄)₂ (**1**). The initial EPR experiments on a polycrystalline sample gave inconsistent results because of the presence of small crystallites in the sample and deterioration with time. Consistent results were only obtained from a finely ground sample of freshly prepared **1**. As shown in Figure 3, the most prominent resonances in the powder spectrum at 300 K are those in the magnetic field region between 250 mT and 400 mT. The first derivative spectrum shows a broad resonance with a peak at around 300 mT and a series of narrower but still ill-defined features in the region around $g = 2$ at 336 mT. The peak at around 300 mT appears to belong to a very broad resonance extending to over 400 mT and centered around $g = 2$. The resonance absorption intensity, in terms of spins with $S = 1/2$ per formula weight, only represents about 5% of the molecules of **1** in the sample.

The interpretation of the spectrum is clarified by its temperature dependence. As shown in Figure 3, the broad resonance with the peak at 300 mT decreases in intensity when the temperature is reduced and is not observed at 120 K. At the same time the linewidths of the resonances in the $g = 2$ region are reduced, and the spectrum becomes better resolved. These resonances are well resolved at about 70 K, with little further improvement down to the lowest temperature reached of 2.5 K. The origin of the resonances observed below 120 K is further clarified by the spectrum of a 5 mM solution of **1** in MeOH after freezing to 120 K, also in Figure 3d. The sharp resonances in the region 332 mT to 340 mT are strongly reminiscent of the spectrum of a nitroxide radical in the solid state and can be simulated with spin Hamiltonian parameters very similar to those of some nitroxide radicals.⁵⁶ The other, rather broader resonances have g -values suggestive of a low-spin ($S = 1/2$) Fe³⁺ complex, and are very similar to those observed from **2**, as described below.

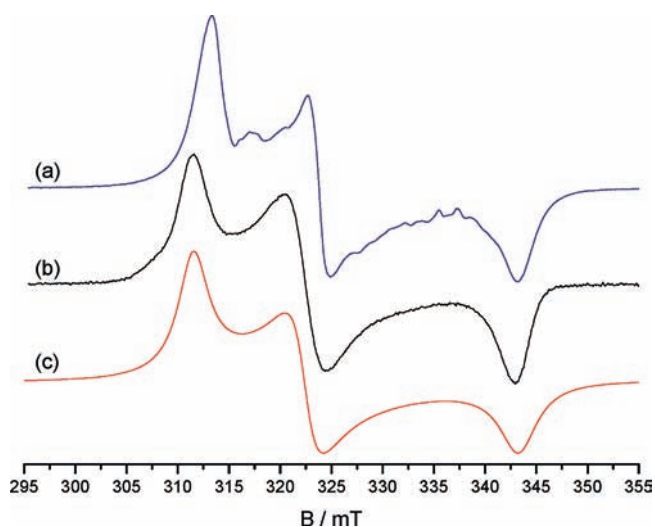


Figure 4. EPR spectra of **2** at 120 K. (a) Polycrystalline powder: microwave frequency 9.434 GHz, receiver gain 1.0×10^4 , 100 kHz modulation amplitude 0.1 mT, microwave power 0.264 mW, magnetic field scan 60 mT/84 s, time constant 81.9 ms. (b) 1.4 mM in CH_2Cl_2 , microwave frequency 9.427 GHz, receiver gain 1.0×10^5 , 100 kHz, modulation amplitude 0.2 mT, microwave power 1.05 mW, magnetic field scan 100 mT/84 s, time constant 81.9 ms. (c) Simulation of the frozen solution spectrum (b) using a Lorentzian line shape of width $18 \times 10^{-4} \text{ cm}^{-1}$ and the g -values given in Table 3.

The temperature dependence of the broad resonance at 300 mT suggests a connection with the temperature dependence of the magnetic moment and therefore the triplet state. The depopulation of the triplet state, located, according to the $\chi_{\text{M}}T$ versus T fit, some 630 cm^{-1} above the $S = 0$ ground state, would be consistent with the gradual disappearance of this resonance below about 200 K. Also consistent with this model is the improved resolution of the remaining resonances in the $g = 2$ region as the temperature is reduced below 200 K, because of the decrease in the interactions with nearby spins. Thus the aforementioned resonance at 300 mT is attributable to resonances within the triplet state. The broadening of the resonances in the $g = 2$ region and attributed to nitroxide radical and Fe^{3+} impurities make it difficult to characterize the probable triplet state resonance further. Resonances around $g = 4$ at 300 K could have given further information on the characteristics of the triplet state, but none were observed in this region.

$[\text{Fe}^{\text{III}}(\text{L}^-)_2](\text{BPh}_4) \cdot 0.5\text{H}_2\text{O}$ (**2**). The X-band EPR spectrum of a finely ground polycrystalline sample of **2** at both 295 and 120 K exhibited features attributable to a spin $S = 1/2$ system with orthorhombic g -values, as shown in Figure 4a. The weak features at fields between the most prominent peaks are attributable to the incompletely randomized orientation of the microcrystals. A more satisfactory spectrum was obtained from a 1.4 mM solution of **2** in CH_2Cl_2 frozen to 120 K, as shown in Figure 4b. A simulation of the frozen solution spectrum using the g -values given in Table 3 is shown in Figure 4c. These g -values are very similar to those of the polycrystalline powder spectrum as also listed in Table 3 and are consistent with expectation for low-spin ($S = 1/2$) Fe^{3+} .

A weak resonance was observed from the polycrystalline powder in the $g \sim 4$ region at high spectrometer gain, as shown in the Supporting Information Figure S11. This “half-field” line is compatible with two low spin Fe(III) ions separated by $\sim 8.5 \text{ \AA}$, a distance consistent with the crystal packing structure. This resonance was

not observed in frozen solution, and it has a different appearance from that expected (and often observed in Fe^{3+} systems) from high spin ($S = 5/2$) Fe^{3+} ions, at $g \sim 4.3$, where $E/D \sim 1/3$.

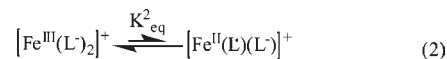
The spectrum of **2** is very similar to that of some low-spin ($S = 1/2$) Fe(III) heme complexes.⁵⁷ The ligand field parameters and the coefficients of the lowest Kramers doublet were calculated from the experimentally determined g -values using the expressions derived by Taylor⁵⁸ and an appropriate choice of signs. With the signs and magnitudes of the g -values as listed in Table 3, we obtain the coefficients of the wave function of the lowest Kramers doublet and the ratio of rhombic to tetragonal splittings, V/Δ , as also listed in Table 3. The signs of the g -values, the coefficients a , b , and c and the relative magnitudes of Δ and V can all be seen to satisfy the various criteria for a proper axis system with z as the tetragonal axis as discussed by Taylor.⁵⁸

The conclusion from ligand field calculations using the EPR g -values is that the ground state has predominantly metal d_{xy} character, with limited covalent bonding to the ligands and a ground state well separated from the higher orbital states. The validity of the ligand field approach can be assessed by comparing the magnitude of the Mössbauer effect quadrupole splitting calculated using the values of a , b , and c with that obtained both experimentally and through DFT calculations. From the expressions derived by Lang and Marshall⁵⁹ we obtain a quadrupole splitting of $\Delta E_{\text{Q}} = 1/2 (QV_{zz}) = 1.48 \text{ mm/s}$, which is in satisfactory agreement with the experimental values obtained from the Mössbauer effect experiments and the theoretical DFT calculations (vide infra).

Electrochemistry. EPR measurements on the formally iron(II) complex, $[\text{Fe}^{\text{II}}(\text{L}^*)_2](\text{BF}_4)$, **1**, provide evidence for a contribution from low-spin iron(III); Figure 3d. Thus, an equilibrium reaction shown in eq 1 probably exists in which the mixed-valent Fe(III) species $[\text{Fe}^{\text{III}}(\text{L}^*)(\text{L}^-)]^{2+}$ is formed via an intramolecular metal-to-ligand charge transfer reaction. These electronically different states could be regarded as a tautomeric pair. However, the equilibrium constant (K_{eq}^1) lies in favor of **1**, thereby making $[\text{Fe}^{\text{II}}(\text{L}^*)_2]^{2+}$ the thermodynamically favored species.



Analogously, the tautomeric pair also can exist as given in eq 2:



where the equilibrium constant heavily favors the $[\text{Fe}^{\text{III}}(\text{L}^-)_2]^{2+}$ form.

Cyclic voltammograms obtained with a GC macroelectrode (1.5 mm diameter) for complex **1** in acetonitrile (0.1 M $[\text{Bu}_4\text{N}](\text{PF}_6)$), exhibit three well-separated, diffusion-controlled, one-electron, reversible processes labeled as **I**, **II**, and **III** in Figure 5a. Their formal reversible potentials ($E_{\text{f}}^{\text{ox}}(n)$, $n = \text{I to III}$) are 0.68, -0.10 , and -1.15 V versus $[\text{FeCp}_2]^{0/+}$, respectively. The peak-to-peak separation ($\Delta E_{\text{p}} = E_{\text{p}}^{\text{ox}} - E_{\text{p}}^{\text{red}}$) for the three processes is similar to that obtained for the reversible oxidation of ferrocene, used as an internal potential reference standard, under the same conditions (e.g., $\Delta E_{\text{p}} = 65 - 75 \text{ mV}$ at scan rate of 0.1 V s^{-1}), demonstrating that all processes are electrochemically reversible (heterogeneous electron-transfer rates for all processes are fast). The chemical reversibility of the three processes (**I**, **II**, and **III**) was also established by noting

Table 3. EPR *g*-Values and Derived Spectral Parameters for **2**

	g_x	g_y	g_z	a	b	c	V/Δ	ΔE_Q (mm/sec)
frozen solution	-2.163	+2.089	-1.963	0.0295	0.0465	0.9925	0.463	1.48
polycrystalline powder	-2.151	+2.081	-1.963	0.0277	0.0441	0.9933	0.474	1.48

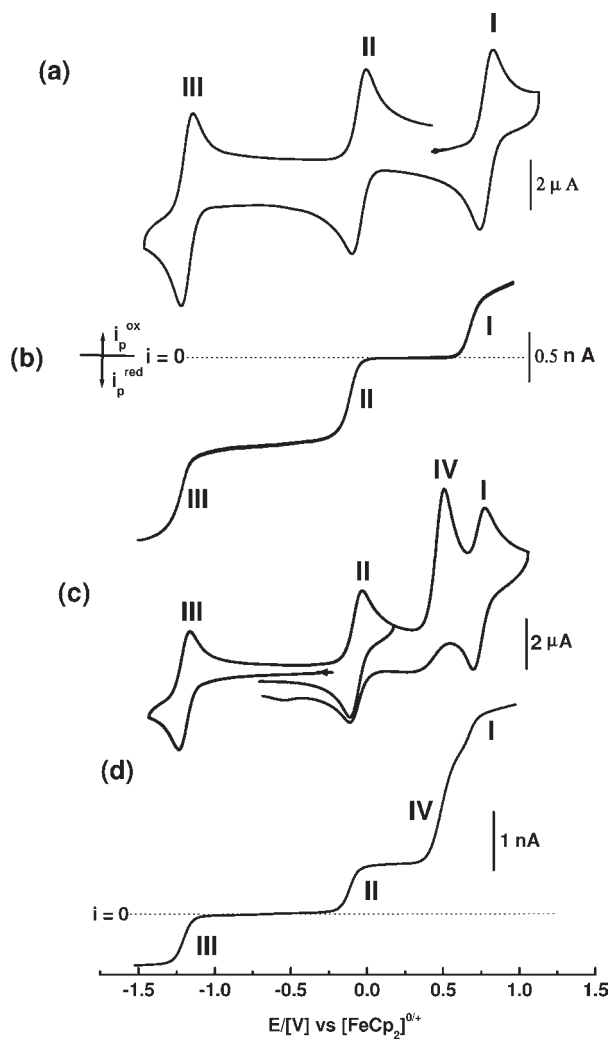
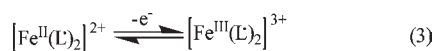


Figure 5. Cyclic (a, c) and linear sweep (b, d) voltammograms obtained with a 1.5 mm diameter glassy carbon disk electrode and 10 μm diameter Pt-microelectrode respectively for 0.6 mM **1** (curves a,b) and 1 mM **2** (curves c,d) in CH_3CN (0.1 M $[\text{Bu}_4\text{N}](\text{PF}_6)$) at a scan rate of 100 mV s^{-1} , 298 K.

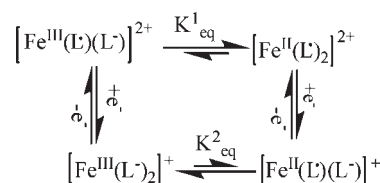
compliances to the diagnostic criteria of cyclic voltammetry³⁹ (oxidation to reduction peak current ratio ~ 1) over the scan rate range (0.1 to 1 V s^{-1}). Analogous voltammetry was found in dichloromethane (0.1 M $[\text{Bu}_4\text{N}](\text{PF}_6)$).

Linear sweep voltammetry with a Pt microelectrode, under near steady-state conditions (Figure 5b), reveals that process I ($E_f^0(\text{I}) = 0.68 \text{ V}$) exhibits positive, that is, oxidation, current. Thus, this process corresponds to a one-electron oxidation, tentatively assigned to a predominantly metal-based Fe(II) to Fe(III) conversion (eq 3).

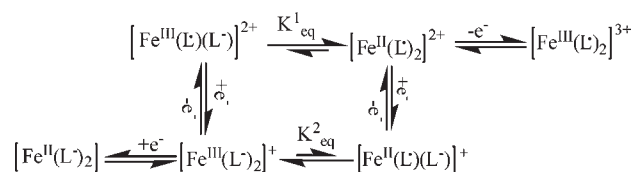


The other two processes (II and III), ($E_f^0(\text{II}) = -0.10$; $E_f^0(\text{III}) = -1.15 \text{ V}$), exhibit negative or reduction currents, and

Scheme 2. Square Scheme Depicting the Different Species Involved in the First Reduction Step (Process II) of **1**



Scheme 3. Square Scheme Depicting the Different Species Involved in the Redox Reactions of **1**



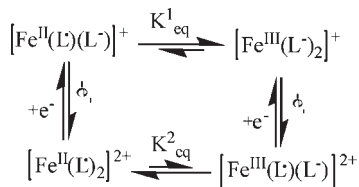
hence are assigned to two consecutive reversible one-electron reduction processes. On the basis of the EPR and Mössbauer findings, the first reduction step (process II) is best described by a square reaction scheme (Scheme 2), while process III is assumed to predominantly involve the redox reaction given in eq 4.

Thus, in summary, the facile reduction process, II, predominantly arises from reduction of one of the nitroxide radical ligands⁶¹ to generate the mixed valence species, $[\text{Fe}^{\text{II}}(\text{L}^\bullet)(\text{L}^-)]^+$. This species then undergoes a fast intramolecular metal-to-ligand charge transfer to yield the thermodynamically favored iron(III) species, $[\text{Fe}^{\text{III}}(\text{L}^-)_2]^+$, as the major product. Consequently, the second reduction step (process III) is mainly the result of a metal-based reduction, in which iron(III) in the monocationic $[\text{Fe}^{\text{III}}(\text{L}^-)_2]^+$ species is reduced to iron(II), to generate the uncharged species $[\text{Fe}^{\text{II}}(\text{L}^-)_2]^0$, as proposed in eq 4.



Taken together, the overall electrochemistry of **1** can be summarized in reaction Scheme 3.

On the basis of the aforementioned redox behavior of **1**, transient cyclic and near steady-state voltammograms obtained for the congener $[\text{Fe}^{\text{III}}(\text{L}^-)_2](\text{BPh}_4)$, **2**, (Figure 5c,d) in CH_3CN (0.1 M $[\text{Bu}_4\text{N}](\text{PF}_6)$) are expected to exhibit two reversible oxidation processes (I and II) at ($E_f^0(\text{I}) = 0.68 \text{ V}$ and $E_f^0(\text{II}) = -0.10$) and one reversible reduction process (III) at $E_f^0(\text{III}) = -1.15 \text{ V}$ versus $[\text{FeCp}_2]^{0/+}$. Very close to this outcome is indeed obtained along with an additional irreversible oxidation process (IV) with a peak potential at $E_p^{\text{ox}} = 0.43 \text{ V}$, associated with oxidation of the BPh_4^- anion. Thus, process (III) is again predominantly metal-based and assigned to reduction of Fe(III) to Fe(II) to give, as proposed for complex **1** (eq 4), the neutral $[\text{Fe}^{\text{II}}(\text{L}^-)_2]$ complex. Since, the formal reversible potential derived from the oxidation process II, $E_f^0(\text{II}) = -0.10 \text{ V}$, has

Scheme 4. Square Scheme Depicting the Different Species Involved in the First Oxidation (Process II) of 2


the same value as the reduction process II in 1, it is assumed to occur as depicted in Scheme 4 which is the reverse of the square reaction Scheme 2. Thus, process II is attributed chiefly to the oxidation of one of the monoanionic forms of oxazolidine-*N*-oxide ligands to generate the mixed-valent dication $[\text{Fe}^{\text{III}}(\text{L}^-)(\text{L}^\bullet)]^{2+}$. This species, as proposed for 1, undergoes intramolecular charge transfer, but in this case from ligand-to-metal, giving rise to the thermodynamically favored iron (II) species, $[\text{Fe}^{\text{II}}(\text{L}^\bullet)_2]^{2+}$, having both ligands in the original radical form as the major species. This latter species, along with the equilibrium concentration of $[\text{Fe}^{\text{III}}(\text{L}^\bullet)(\text{L}^-)]^{2+}$ species, are further oxidized via the oxidation process I ($E^0_{\text{f}}(\text{I}) = 0.68$ V), as proposed for complex 1 in eqs 1 and 3), to produce the tricationic iron(III) species, $[\text{Fe}^{\text{III}}(\text{L}^\bullet)_2]^{3+}$.

The combination of electrochemical results from the two iron complexes 1 and 2 clearly establish that both share the same primary voltammetric characteristic of having three reversible processes with almost identical E^0_{f} values. The difference in ligands and central metal oxidation levels implies that different equilibrium constants (K^1_{eq} and K^2_{eq}) are required to accommodate the structural changes induced by the intramolecular charge transfer redox based interconversion of the compounds. Furthermore, the data highlight that both the oxazolidine-*N*-oxide ligand and BPh_4^- counteranion are “non-innocent” and that the former is responsible for the redox-induced structural changes associated with the square reaction processes in Schemes 3 and 4. Importantly, formation of the monocation $[\text{Fe}^{\text{III}}(\text{L}^-)_2]^+$ from the parent $[\text{Fe}^{\text{II}}(\text{L}^\bullet)_2]^{2+}$ complex via a fast, reductively induced intermolecular metal-to-ligand charge transfer that occurs upon one-electron reduction of the ligand is counterintuitive. However, a similar finding was reported for a series of bis(α -diimine) nickel complexes, $[\text{Ni}(\text{L}^\bullet)_2]^z$ ($z = 0, 1+, 2+$) containing the conceptually related π radical anion, 2-phenyl-1,4-bis(isopropyl)-1,4-diazabutadiene (L^\bullet).⁶² Of particular relevance is the neutral complex, $[\text{Ni}^{\text{II}}(\text{L}^\bullet)_2]$, which, upon oxidation with 1 equiv of $[\text{Fe}^{\text{III}}\text{Cp}_2](\text{PF}_6)$, produced the paramagnetic $[\text{Ni}^{\text{I}}(\text{L}^\bullet)_2](\text{PF}_6)$, through an analogous “oxidatively induced reduction of the central nickel ion”. This process also could be described in terms of a square scheme.

Similarly, although the overall redox behavior for $[\text{Fe}^{\text{II}}(\text{L}^\bullet)_2](\text{BF}_4)_2$ mimics that reported for the conceptually related iron(II) complex, $[\text{Fe}^{\text{II}}(\text{L}')_2](\text{PF}_6)_2$, $\text{L}' = 2,6$ -bis[1-(4-methoxyphenylimino)ethyl]pyridine,⁶³ in the sense that both complexes exhibit one metal-based reversible oxidation and two reversible reduction processes, the assignment of the reduction processes and their formal potentials, in both complexes, are different. In the complex, $[\text{Fe}^{\text{II}}(\text{L}')_2](\text{PF}_6)_2$, the two reduction processes ($E^0_{\text{f}}(1, 2) = -1.31$ and -1.66 V vs $[\text{FeCp}_2]^{0/+}$) have been assigned to simple ligand-based reductions, whereas in 1 the first reduction process (II) is predominantly occurring by a square scheme, leading to a ligand-based reduction that is

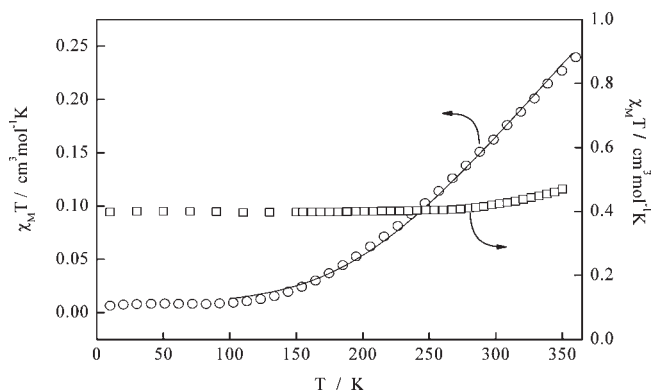


Figure 6. Plots of $\chi_{\text{M}}T$ versus T , per mol, for 1 (open circles) and per mol for 2 (open squares). The solid line is the best fit for 1 calculated using a $S = 1/2$ dimer model with $g = 2.0$ and $J = -315$ cm^{-1} (see text).

concurrent with oxidation of the central metal (Fe(II) to Fe(III)), while the second reduction process (III) predominantly corresponds to a metal-based reaction following a significant level of conversion of Fe(III) to Fe(II). In addition, the very low value of the reversible potential of reduction process II ($E^0_{\text{f}} = -0.10$ V) compared to $E^0_{\text{f}}(1) = -1.31$ V for the Wieghardt system, suggests that addition of the first electron into the singly occupied molecular orbital (SOMO) of the oxazolidine-*N*-oxide ligand is much more facile than is the case with the diimine ligand. Thus, the overall similarity in the voltammetric redox behavior, but distinctly different formal potential of the reduction processes in both complexes reflects a significant difference in ligand σ -donating and π -accepting properties. In this regard, the oxazolidine-*N*-oxide ligand is considered to have lower σ -donating and higher π -accepting capabilities than the diimine ligand.⁶

Magnetic Susceptibilities and Mössbauer spectroscopy.

Direct current (dc) magnetic susceptibility measurements were performed on two freshly prepared samples of $[\text{Fe}^{\text{II}}(\text{L}^\bullet)_2](\text{BF}_4)_2$, 1, in the 5–350 K range under an applied field of 5 kOe, with the same results obtained (Figure 6). The $\chi_{\text{M}}T$ value of 0.23 cm^3 K mol^{-1} ($\mu_{\text{eff}} = 1.36$ μ_{B}), at 350 K, decreases more or less linearly down to a $\chi_{\text{M}}T$ value of 0.06 cm^3 K mol^{-1} at ~ 200 K, whereupon it then decreases very gradually down to a final $\chi_{\text{M}}T$ value of 0.007 cm^3 K mol^{-1} ($\mu_{\text{eff}} = 0.24$ μ_{B}) at 5 K. At the temperature of the crystal structure, 123 K, $\chi_{\text{M}}T$ is ~ 0.01 cm^3 K mol^{-1} ($\mu_{\text{eff}} \sim 0.28$ μ_{B}), typical of LS Fe^{II} values that have second order Zeeman contributions making the observed moment small and positive. The magnetic data fitted well to an exchange-coupled $S = 1/2$ dimer model employing the spin Hamiltonian $-2J\mathbf{S}_1 \cdot \mathbf{S}_2$ using $g = 2.00$ and $J = -315$ cm^{-1} , indicative of strong antiferromagnetic coupling between the two L radicals across the $S = 0$ Fe^{II} low-spin center. Further discussion is given in relation to the DFT calculations, below.

The $\chi_{\text{M}}T$ plot for $[\text{Fe}^{\text{III}}(\text{L}^-)_2](\text{BPh}_4)_2$, 2, shown in Figure 6, is Curie-like and has a value compatible with a $S = 1/2$ ground state, the latter being in accordance with a t_{2g}^5 low spin Fe(III). The low symmetry ligand field around Fe(III) causes a large splitting of the ${}^2T_{2g}$ parent state, in accordance with the Δ/λ and V/λ values deduced from the EPR spectra (estimate ~ 3000 cm^{-1}), thus rendering $\chi_{\text{M}}T$ independent of temperature. There is a hint of a gradual spin transition starting above ~ 270 K.

The room temperature Mössbauer spectrum of $[\text{Fe}^{\text{II}}(\text{L}^\bullet)_2](\text{BF}_4)_2$, 1, shows an asymmetric doublet (Figure 7). Although the major contribution, and its parameters, was quite

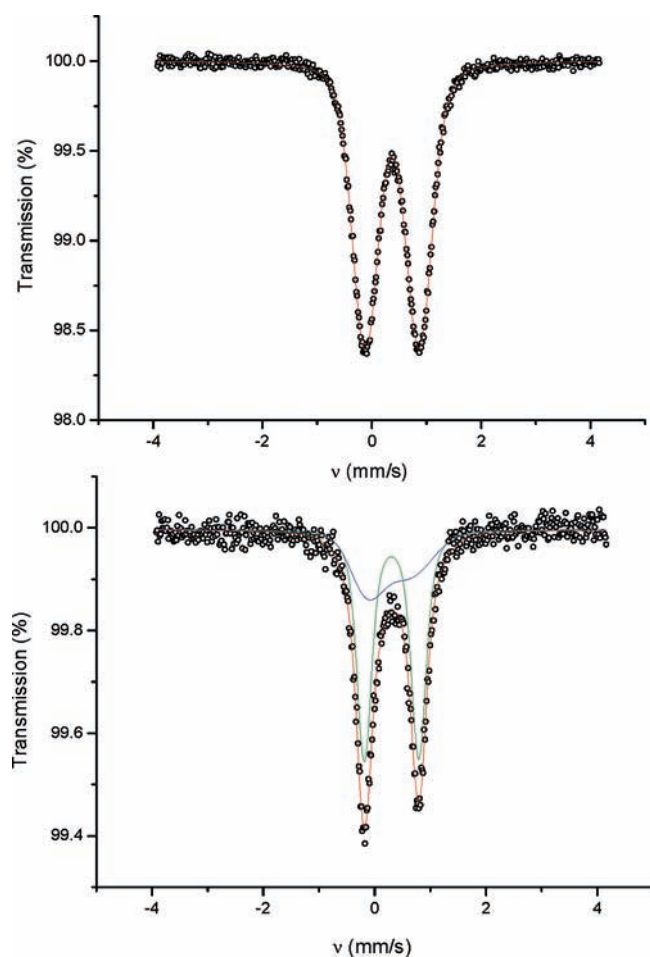


Figure 7. Zero field ^{57}Fe Mössbauer spectra of complex **1** recorded at 78 K (top) and at room temperature (bottom) with the solid red line representing the best fit obtained with parameters: IS = 0.37(1) mm/s, $|\Delta E_Q|$ = 0.98(1) mm/s at 78 K; IS = 0.30(3) mm/s and $|\Delta E_Q|$ = 0.98(1) mm/s (Area 66%), IS = 0.17(3) mm/s and $|\Delta E_Q|$ = 0.76(12) mm/s (Area 34%) at room temperature. The solid red line (bottom) is a fit of the sum of two Voigtians (solid green and blue lines).

clear, there were a variety of ways in which the asymmetry could be accommodated depending on whether one allows unequal line intensities or linewidths or other asymmetric lineshapes. We believe that the most physically realistic solution is to fit the spectrum to the sum of two Voigtians, with a correlation, δ_1 , being allowed between the isomer shift and the quadrupole splitting. This fit, which is shown in Figure 7, with the parameters in Table 4, also had the equal lowest χ^2 value.

At 78 K, the spectrum had become symmetrical (Figure 7) and it was fitted to a single Voigtian with the parameters given in Table 4. The quadrupole splitting is unchanged from the value for the well-resolved part of the room temperature spectrum. One question is how to interpret the poorly resolved part of the room temperature spectrum? We note that one would normally expect a thermal shift of approximately -0.12 mm/s in changing from 78 K to room temperature, but the change to the well-resolved part is only 0.07 mm/s. However, if one takes the weighted mean of the isomer shifts of the two components at 0.26 mm/s, then the thermal shift is correct, within error. This fact, together with the appearance of the clean spectrum at 78 K, suggests that the poorly resolved part is due to a very closely

Table 4. Fitted Parameters to the Mössbauer Spectra of $[\text{Fe}^{\text{II}}(\text{L}^*)_2](\text{BF}_4)_2$ (**1**) and $[\text{Fe}^{\text{III}}(\text{L}^-)_2](\text{BPh}_4)$ (**2**) at Room Temperature and 78 K

sample/temperature	IS (mm/s)	δ_1	QS (mm/s)	σ_Δ (mm/s)	area (%)
1/ RT	0.30(3)	0.01(3)	0.98(1)	0.17(2)	66
	0.17(3)	0.09(3)	0.76(12)	0.6(2)	34
1/ 78 K	0.37(1)	0.002(3)	0.98(1)	0.39(1)	100
2/ RT	0.18(1)		1.36(1)		100
2/ 78 K	0.25(1)		1.40(1)		100

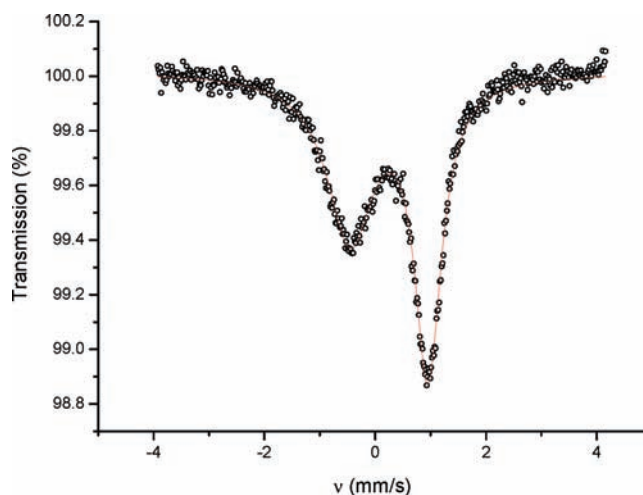


Figure 8. Zero field ^{57}Fe Mössbauer spectrum of a powdered sample of complex **2** recorded at 78 K. The solid red line represents the best fit obtained with two Lorentzian lines yielding mean parameters: IS = 0.25(1) mm/s, $|\Delta E_Q|$ = 1.40 mm/s. The peak areas were the same to within 1%.

related configuration for the iron atoms which condenses into the major configuration as the temperature is lowered. The Mössbauer parameters, for **1**, are compatible with values observed for LS Fe(II). The isomer shift and quadrupole splitting values calculated by DFT methods are discussed below.

The Mössbauer spectrum for a powdered sample of **2**, at 78 K, shows a very asymmetric doublet (Figure 8), a feature often observed for LS Fe^{III} compounds. A sample of crystallite needles showed the same line shape and parameter values. The fitted parameters are typical of LS Fe^{III} and in good agreement with the values calculated by DFT methods, vide infra. The room temperature spectrum was also asymmetrical and had a small change in isomer shift (-0.06 mm/s) and in quadrupole splitting (-0.04 mm/s) compared to 78 K, the latter reflecting crystal field effects (Supporting Information, Figure SI2).

From an oxidation state point of view, the low temperature χ_{MT} values for **1** indicate a close to diamagnetic ground state which could originate from a number of Fe {oxidation state/spin state}, and ligand {redox state/spin state} scenarios. The combined structural and physicochemical data obtained support a large antiferromagnetic interaction between the two coordinated radicals mediated by the diamagnetic low spin Fe(II). The nitroxide N–O bond lengths in $[\text{Fe}^{\text{II}}(\text{L}^*)_2](\text{BF}_4)_2$ and subsequent DFT calculations indicate a degree of overlap between the ligand centered SOMOs and the metal t_{2g} orbitals suggesting antiferromagnetic coupling between the coordinated radicals

Table 5. Calculated and Experimental Bond Distances and Angles for **1 and **2**^a**

	calc (1).	exp (1).	calc (2).	exp (2).
Fe–N(1)	2.001	1.973	1.965	1.964
Fe–N(2)	1.986	1.982	1.996	1.996
Fe–N(1')	2.001	1.973	1.965	1.964
Fe–N(2')	1.986	1.982	1.996	1.996
Fe–O(1)	1.883	1.876	1.888	1.856
Fe–O(1')	1.883	1.876	1.888	1.856
N(3)–O(1)	1.322	1.317	1.393	1.411
N(3')–O(1')	1.322	1.317	1.393	1.411

^aExperimental values given for the cation associated with Fe1.

mediated by the diamagnetic LS Fe(II), as observed in the susceptibility studies. Diamagnetic LS Fe(II) ions (t_{2g}^6) have been shown, previously, to act as superexchange couplers between HS Fe(III) ions ($t_{2g}^3 e_g^2$) in compounds such as Prussian blue,⁶⁴ the heptanuclear complex $[\text{Fe}^{\text{II}}\{\text{CNFe}^{\text{III}}(\text{L})\}_6]\text{Cl}_2 \cdot 6\text{H}_2\text{O}$ (where L = bis(3-salicylideneaminopropyl)methylamine),⁶⁵ and in the mixed-valent trinuclear complex $[\text{Fe}^{\text{II}}\text{Fe}^{\text{III}}_2(\text{pzNTR})_6](\text{ClO}_4)_2 \cdot \text{CH}_3\text{OH}$ (where pzNTR is deprotonated *N-tert-butyl- α -3-pyrazolynitron*).⁶⁶ Weak ferromagnetic exchange was observed in these cases and was attributed to a mixing of the excited configurations (resulting from charge transfer between the low-spin Fe(II) and the high-spin Fe(III)) with the ground configuration. Interestingly the $[\text{Zn}^{\text{II}}(\text{L}^\bullet)_2](\text{CF}_3\text{SO}_3)_2$ ¹⁷ analogue of **1** shows a much smaller exchange between intramolecular nitroxide spins ($J = -0.64 \text{ cm}^{-1}$, indicative of two weakly coupled spins) than for complex **1**, with $J = -315 \text{ cm}^{-1}$. It is interesting to contemplate the origin of this large difference in structurally similar species. It may relate to the availability of the empty e_g set in complex **1** as compared to $[\text{Zn}^{\text{II}}(\text{L}^\bullet)_2](\text{CF}_3\text{SO}_3)_2$. However, the differences in d-orbital energies and sizes for the LS Fe^{II} and Zn^{II} ions are important. The superexchange pathway in **1** has to go through the π -symmetry orbitals, t_{2g} , since the two L[•] ligands are π -radicals. The t_{2g} orbital sets are filled in both the Fe^{II} and the Zn^{II} derivatives but the Zn^{II} d-orbitals will be more contracted and lower in energy because of its higher effective nuclear charge. Therefore, the overlap with the ligand SOMOs and consequently the coupling between the unpaired L[•] electrons is smaller in the Zn case.

For the monocation **2**, the data are all consistent with both ligands being in the diamagnetic L⁻ forms, with Fe in the III oxidation state, and low spin, thus yielding $[\text{Fe}^{\text{III}}(\text{L}^-)_2](\text{BPh}_4) \cdot 0.5\text{H}_2\text{O}$, with a $S = 1/2$ metal based ground state. EPR spectra and DFT calculations indicate a small spin density occurring on the ligand donor atoms.

DFT Calculations. Broken symmetry (BS) DFT calculations of the untruncated dication $[\text{Fe}(\text{L}^\bullet)_2]^{2+}$ and the monocation $[\text{Fe}(\text{L}^-)_2]^+$ were conducted to further elucidate their electronic structures (Table 5). The broken symmetry formalism has been shown to be a good approximation for the multireference ground state of open-shell diradical coordination compounds.^{67,68} The ground state geometry of the dication $[\text{Fe}(\text{L}^\bullet)_2]^{2+}$ was optimized by using the BP86 functional assuming a spin-unrestricted BS(1,1) mS = 0 model to account for the experimentally determined diamagnetic ground state. Complex **2** was treated as a spin-unrestricted doublet.

Electronic ground state calculations on the optimized structures were carried out at the B3LYP level of DFT. For **1**, three possible diamagnetic models were taken into consideration: a

simple closed-shell spin-restricted model, an open-shell BS(1,1) model corresponding to two ligand radicals coupled antiferromagnetically to each other via superexchange mediated by a low-spin ferrous ion, and an open-shell BS(2,2) model corresponding to two ligand radicals coupled antiferromagnetically to an intermediate-spin ferrous ion. The BS(1,1) solution was found to be the electronic ground state and is 15.9 kcal/mol more stable than the closed-shell solution establishing the singlet-diradical character of the complex. Reassuringly, the BS(2,2) approach converged back to the BS(1,1) solution. A qualitative molecular orbital diagram for $[\text{Fe}(\text{L}^\bullet)_2]^{2+}$ is shown in Figure 9. Three doubly filled orbitals with predominant metal d character comprise the t_{2g} set of the low-spin ferrous ion, while two unoccupied d orbitals can be found at higher energy defining the e_g set. Additionally, two ligand centered SOMOs of opposite spin orientation can be identified. Antiferromagnetic coupling between these two orbitals is mediated via a very small contribution of one of the metal t_{2g} orbitals giving rise to a relatively small mutual spatial overlap of 0.24 indicating relatively weak coupling. The spin density population analysis highlights the antiparallel spin alignment between the two ligands (Figure 9).

For **2**, the qualitative MO diagram shown in Figure 10 indicates that the two ligand centered orbitals are doubly occupied, not quite degenerate, and below the singly occupied metal t_{2g} orbital (SOMO). The lowest unoccupied molecular orbital (LUMO) and the highest energy orbital are metal based and of e_g character. The spin density population analysis shows that the unpaired electron is localized predominantly on the Fe^{III} center, but with significant spin on the nitroxide oxygen atoms.

Mössbauer spectral parameters for **1** were also computed using DFT methods to further calibrate the computational results against experimental data. The calculated isomer shift of 0.41 mm s⁻¹ and quadrupole splitting of 0.53 mm s⁻¹ provide reasonably good agreement with the experimental values of 0.37 mm s⁻¹ and 0.98 mm s⁻¹, respectively, and are fully consistent with a low-spin ferrous ion. Similarly, for **2**, the calculated isomer shift of 0.26 mm/s and quadrupole splitting of 1.34 mm/s are in very good agreement with the experimental values of 0.25 and 1.40 mm/s, respectively.

CONCLUSIONS

The two congeners **1** and **2**, containing tridentate dipyriddylnitroxide ligands, have been synthesized and structurally characterized. The six-coordinate structures are very similar, and the NO bond lengths are very sensitive to the redox state of the ligand. Complex **1**, $[\text{Fe}^{\text{II}}(\text{L}^\bullet)_2](\text{BF}_4)_2$, contains the neutral radical form, L[•], with the iron in the low-spin Fe(II) state while **2**, having a different counteranion, contains the reduced form L⁻, namely, $[\text{Fe}^{\text{III}}(\text{L}^-)_2](\text{BPh}_4) \cdot 0.5\text{H}_2\text{O}$. Electrochemical studies on both compounds support the existence of **1** and **2** in solution, and, importantly, the inter-relations between the various metal and ligand redox states, inherent in redox reactions of **1** and **2**, are fully described in terms of square reaction schemes. In addition, the overall redox behavior of **1** and **2** is compared to more simple ligand-based redox reactions that were applicable to other iron bis-imino radical species, reported recently by one of the authors, as well as to Ni-diimine radical complexes that showed “oxidatively induced reduction of the central nickel ion”. Certainly, the ligand, L, and the anion BPh₄⁻ are “non-innocent” in the chemistry, electrochemistry, and physical properties described here.

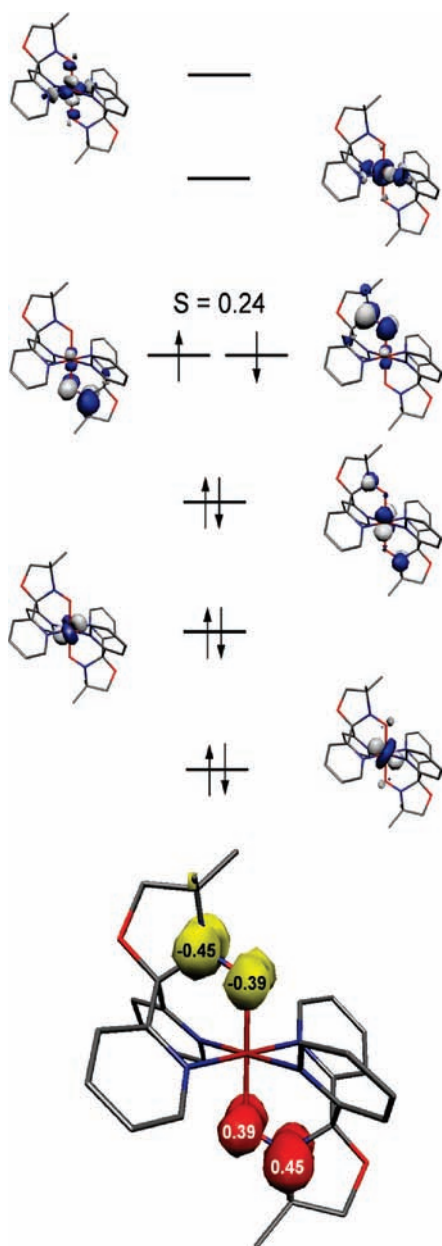


Figure 9. Top: Qualitative molecular orbital diagram for $[\text{Fe}^{\text{II}}(\text{L}^*)_2]^{2+}$ obtained from a B3LYP DFT calculation. Bottom: Spin density plot obtained from a Mulliken population analysis. Positive spin density is shown in red and negative spin density is shown in yellow.

Magnetic, Mössbauer, IR, and EPR spectral studies, supported by DFT calculations, give further support for these ligand redox states in the crystalline state, and **1** provides a rare example of very strong antiferromagnetic coupling between the L^* spins across a $S = \text{Fe}(\text{II})$ low-spin center. In contrast, $S = 1/2$ paramagnetic behavior is noted for **2** with the spin arising from the low spin $\text{Fe}(\text{III})$ center. A final comment and caution is worth making on the strong antiferromagnetic coupling observed in the magnetic data for **1**. Qualitative arguments were given, above, in terms of differences in energy and size for the LS Fe^{II} center in **1** and the Zn^{II} center in the Zn analogue, the latter showing very weak coupling. It might be expected that DFT calculations of the singlet–triplet gap, that is, $2J$, would resolve the situation. However, the energies and J values

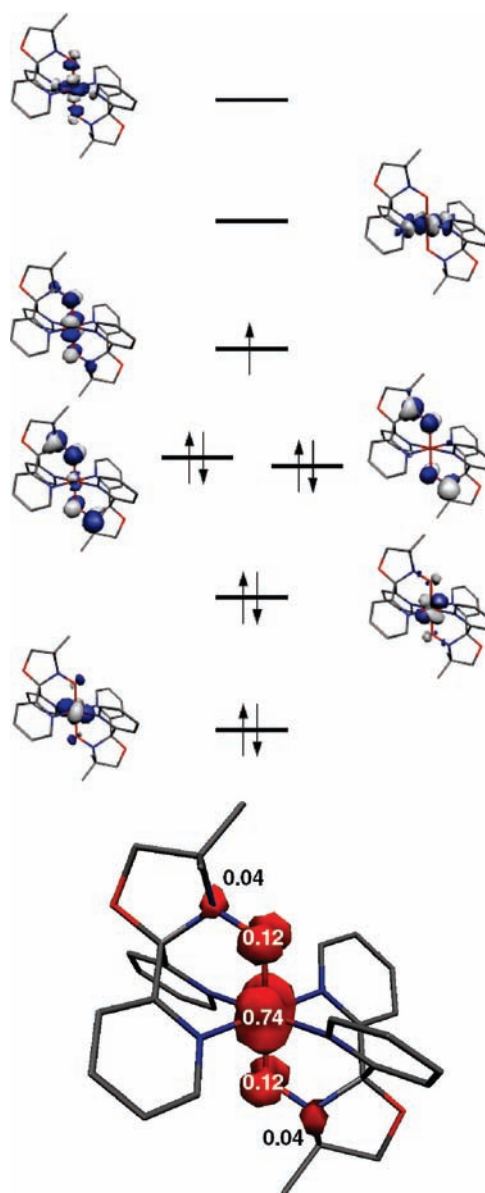


Figure 10. Top: Qualitative molecular orbital diagram for $[\text{Fe}^{\text{III}}(\text{L}^-)_2]^+$ obtained from a B3LYP DFT calculation. Bottom: Spin density plot obtained from a Mulliken population analysis. Positive spin density is shown in red.

computed depend very much on the basis functions used for the calculations. Pure DFT such as BP86 strongly favors singlet states, while Hartree–Fock favors high-spin states. Hybrid functions therefrom, such as B3LYP, yield an outcome that depends on the amount of Hartree–Fock exchange mixed in to the DFT functions. In the case of complex **1**, for example, the BP86 approach yields the singlet lowest and J of between -400 to -800 cm^{-1} while B3LYP slightly prefers the triplet state being lowest and J of $+100$ to $+200 \text{ cm}^{-1}$. It is best to view such calculated J values as ballpark measures, namely, weak or strong.

■ ASSOCIATED CONTENT

S Supporting Information. Plots of EPR spectrum of **2** at “half field”, Figure S11; Mössbauer spectra of **2** at RT and 78 K,

Figure S12; CIF files for **1** and **2**. This material is available free of charge via the Internet at <http://pubs.acs.org>.

AUTHOR INFORMATION

Corresponding Author

*E-mail: keith.murray@monash.edu (K.S.M.).

ACKNOWLEDGMENT

We thank the Australian Research Council (ARC) for Discovery and LIEF grants (to K.S.M. and D.W.L.).

REFERENCES

- (1) (a) Chirik, P. J.; Wieghardt, K. *Science* **2010**, *327*, 794. (b) Bowman, A. C.; Milsman, C.; Bill, E.; Lobkovsky; Weyermüller, T.; Wieghardt, K.; Chirik, P. J. *Inorg. Chem.* **2010**, *49*, 6110. (c) Bart, S. C.; Lobkovsky, E.; Chirik, P. J. *J. Am. Chem. Soc.* **2004**, *126*, 13794.
- (2) (a) Pierpont, C. G.; Lange, C. W. *Prog. Inorg. Chem.* **1994**, *41*, 331. (b) Chaudhuri, P.; Wieghardt, K. *Prog. Inorg. Chem.* **2001**, *50*, 151. (c) Chaudhuri, P.; Verani, C. N.; Bill, E.; Bothe, E.; Weyhermüller, T.; Wieghardt, K. *J. Am. Chem. Soc.* **2001**, *123*, 2213. (d) Sproules, S.; Wieghardt, K. *Coord. Chem. Rev.* **2010**, *254*, 1358.
- (3) (a) Jazdzewski, B. A.; Tolman, W. B. *Coord. Chem. Rev.* **2000**, *200–202*, 633. (b) Stubbe, J.; van der Donk, W. A. *Chem. Rev.* **1998**, *98*, 706.
- (4) Miller, J. S.; Calabrese, J. C.; Epstein, A. J.; Bigelow, R. W.; Zhang, J. H.; Reiff, W. M. *J. Chem. Soc., Chem. Commun.* **1986**, 1026.
- (5) Caneschi, A.; Gatteschi, D.; Sessoli, R.; Rey, P. *Acc. Chem. Res.* **1989**, *22*, 392.
- (6) Caneschi, A.; Gatteschi, D.; Rey, P. *Prog. Inorg. Chem.* **1991**, *39*, 331.
- (7) (a) *Spin Labelling Theory and Applications*; Berliner, L. J., Ed.; Academic Press: New York, 1976–1979; Vols. 1 and 2. (b) Keana, J. F. W. *Chem. Rev.* **1978**, *78*, 37.
- (8) Kinoshita, M.; Turek, P.; Tamura, M.; Nozawa, K.; Shiomi, D.; Nakazawa, Y.; Ishikawa, M.; Takahashi, M.; Awaga, K.; Inabe, T.; Maruyama, Y. *Chem. Lett.* **1991**, 1225.
- (9) (a) Inoue, K.; Iwamura, H. *J. Am. Chem. Soc.* **1994**, *116*, 3173. Inoue, K.; Iwamura, H. *Adv. Mater.* **1996**, *8*, 73. (b) Inoue, K.; Hayamizu, T.; Iwamura, H.; Hashizume, D.; Ohashi, Y. *J. Am. Chem. Soc.* **1996**, *118*, 1803.
- (10) Caneschi, A.; Gatteschi, D.; Lalioti, N.; Sangregorio, C.; Sessoli, R.; Venturi, A.; Vindigni, A.; Rettori, A.; Pini, M. G.; Novak, M. A. *Angew. Chem., Int. Ed.* **2001**, *40*, 1760.
- (11) (a) Caneschi, A.; Ferraro, F.; Gatteschi, D.; Rey, P.; Sessoli, R. *Inorg. Chem.* **1990**, *29*, 4217. Luneau, D.; Risoan, G.; Rey, P.; Grand, A.; Caneschi, A.; Gatteschi, D.; Laugier, J. *Inorg. Chem.* **1993**, *32*, 5616. (b) Francese, G.; Romero, F. M.; Neels, A.; Stoeckli-Evans, H.; Decurtins, S. *Inorg. Chem.* **2000**, *39*, 2087. (c) Okazawa, A.; Hashizume, D.; Ishida, T. *J. Am. Chem. Soc.* **2010**, *132*, 11516.
- (12) Luneau, D.; Rey, P. *Magnetism: A Supramolecular Function*; Kahn, O., Ed.; NATO ASI Series 484; Kluwer Academic Publishers: Dordrecht, The Netherlands, 1996; p 431.
- (13) Luneau, D.; Romero, F. M.; Ziessel, R. *Inorg. Chem.* **1998**, *37*, 5078.
- (14) (a) Luneau, D.; Rey, P. *Mol. Cryst. Liq. Cryst.* **1995**, *273*, 81. (b) Fegy, K.; Luneau, T.; Ohm, C.; Paulsen, P.; Rey, P. *Angew. Chem., Int. Ed.* **1998**, *37*, 1270.
- (15) Nihei, M.; Maeshima, T.; Kose, Y.; Oshio, H. *Polyhedron* **2007**, *26*, 1993.
- (16) Wang, X.-L.; Yang, P.-P.; Li, Z.-W.; Li, L.-C.; Liao, D.-Z. *Inorg. Chim. Acta* **2009**, *362*, 1901.
- (17) Ito, A.; Nakano, Y.; Urabe, M.; Tanaka, H.; Shiro, M. *Eur. J. Inorg. Chem.* **2006**, 3359.
- (18) (a) *Spin-Crossover in Transition-Metal Compounds*; Gütlich, P., Goodwin, H. A., Eds.; Springer: Berlin, Germany, 2004; Topics in Current Chemistry, Vols. 233–235. (b) An example of coupled electron-transfer and spin-crossover in an iron diimine complex is: Khusniyarov, M. M.; Weyermüller, T.; Bill, E.; Wieghardt, K. *Angew. Chem., Int. Ed.* **2008**, *47*, 1228. (c) Sutter, J.-P.; Fettouhi, M.; Li, L.; Michaut, C.; Ouahab, L.; Kahn, O. *Angew. Chem., Int. Ed.* **1996**, *35*, 2113.
- (19) Examples of Fe(II) spin crossover with N,O donor ligands: (a) Weber, G.; Kaps, E. S.; Desplanches, C.; Létard, J.-F.; Achterhold, K.; Parak, F. G. *Eur. J. Inorg. Chem.* **2008**, 4891. (b) Weber, G.; Kaps, E.; Weigand, J.; Carbonera, C.; Létard, J.-F.; Achterhold, K.; Parak, F. G. *Inorg. Chem.* **2008**, *47*, 487. (c) Weber, B.; Jäger, E.-G. *Eur. J. Inorg. Chem.* **2009**, 465.
- (20) (a) Sheldrick, G. M. *SHELXL-97, program for refinement of crystal structures*; University of Göttingen: Göttingen, Germany, 1997; (b) Spek, A. L. *Acta Crystallogr., Sect. A* **1990**, *46*, C34.
- (21) Neese, F. *ORCA, an ab initio, DFT and Semiempirical Electronic Structure Package*, Version 2.7, Revision 0; Institut für Physikalische und Theoretische Chemie, Universität Bonn: Bonn, Germany, 2010.
- (22) Perdew, J. P. *Phys. Rev. B* **1986**, *33*, 8822.
- (23) Becke, A. D. *J. Chem. Phys.* **1986**, *84*, 4524.
- (24) Perdew, J. P. *Phys. Rev. B* **1986**, *34*, 7406.
- (25) Becke, A. D. *J. Chem. Phys.* **1993**, *98*, 5648.
- (26) Lee, C. T.; Yang, W. T.; Parr, R. G. *Phys. Rev. B* **1988**, *37*, 785.
- (27) Schäfer, A.; Huber, C.; Ahlrichs, R. *J. Chem. Phys.* **1994**, *100*, 5829.
- (28) Eichkorn, K.; Treutler, O.; Öhm, H.; Häser, M.; Ahlrichs, R. *Chem. Phys. Lett.* **1995**, *240*, 283.
- (29) Eichkorn, K.; Treutler, O.; Öhm, H.; Häser, M.; Ahlrichs, R. *Chem. Phys. Lett.* **1995**, *242*, 652.
- (30) Eichkorn, K.; Weigend, F.; Treutler, O.; Ahlrichs, R. *Theor. Chem. Acc.* **1997**, *97*, 119.
- (31) Neese, F.; Wenmohs, F.; Hansen, A.; Becker, U. *Chem. Phys.* **2009**, *356*, 98.
- (32) Ginsberg, A. P. *J. Am. Chem. Soc.* **1980**, *102*, 111.
- (33) Noodleman, L.; Peng, C. Y.; Case, D. A.; Mouesca, J. M. *Coord. Chem. Rev.* **1995**, *144*, 199.
- (34) Kirchner, B.; Wennmohs, F.; Ye, S.; Neese, F. *Curr. Opin. Chem. Biol.* **2007**, *11*, 134.
- (35) *Molekel, Advanced Interactive 3D-Graphics for Molecular Sciences*; available under <http://www.cscs.ch/molkel/>.
- (36) Sinnecker, S.; Slep, L. D.; Bill, E.; Neese, F. *Inorg. Chem.* **2005**, *44*, 2245.
- (37) Neese, F. *Inorg. Chim. Acta* **2002**, *337*, 181.
- (38) Nafady, A.; O'Mullane, A. P.; Bond, A. M.; Neufeld, A. K. *Chem. Mater.* **2006**, *18*, 4375.
- (39) Geiger, W. E. In *Laboratory Techniques in Electrochemistry*, 2nd ed.; Kissinger, P. T.; Heineman, W. R., Eds.; Marcel Dekker: New York, 1996; Chapter 23.
- (40) Wertz, J. E.; Orton, J. W.; Auzins, P. *Faraday Discuss.* **1961**, *31*, 140.
- (41) Hanson, G. R.; Gates, K. E.; Noble, C. J.; Griffin, M.; Benson, S. *J. Inorg. Biochem.* **2004**, *98*, 903.
- (42) Guionneau, P.; Marchivie, M.; Bravic, G.; Létard, J.-F.; Chasseau, D. *Top. Curr. Chem.* **2004**, *234*, 97.
- (43) Kim, Y.; Feng, X.; Lippard, S. J. *Inorg. Chem.* **2007**, *46*, 6099.
- (44) Caneschi, A.; Laugier, J.; Rey, P. *J. Chem. Soc., Perkin Trans.* **1987**, 1077.
- (45) Wang, X.-L.; Yang, P.-P.; Li, Z.-W.; Li, L.-C.; Lia, D.-Z. *Inorg. Chim. Acta* **2009**, 1901.
- (46) Fujino, M.; Hasegawa, S.; Akutsu, H.; Yamada, J.; Nakatsui, S. *Polyhedron* **2007**, *26*, 1989.
- (47) Porter, L. C.; Doedens, R. J. *Inorg. Chem.* **1985**, *24*, 1007.
- (48) Porter, L. C.; Dickman, M. H.; Doedens, R. J. *Inorg. Chem.* **1986**, *25*, 678.
- (49) Matsunaga, P. T.; McCall, D. T.; Carducci, M. D.; Doedens, R. J. *Inorg. Chem.* **1990**, *29*, 1655.
- (50) Porter, L. C.; Dickman, M. H.; Doedens, R. J. *Inorg. Chem.* **1988**, *27*, 1548.

- (51) Kinoshita, H.; Akutsu, H.; Yamada, J.-I.; Nakatsuji, S. *Inorg. Chim. Acta* **2008**, *361*, 4159.
- (52) Dickman, M. H. *Acta Crystallogr., Sect. C* **1997**, *53*, 1192.
- (53) Ahlers, C.; Dickman, M. H. *Inorg. Chem.* **1998**, *37*, 6337.
- (54) Jaitner, P.; Huber, W. *J. Organomet. Chem.* **1983**, *259*, C1.
- (55) Jaitner, P.; Huber, W.; Gieren, A.; Betz, H. *J. Organomet. Chem.* **1986**, *311*, 379.
- (56) Dzuba, S. A. *Phys. Lett. A* **1996**, *213*, 77.
- (57) Walker, F. A. *Coord. Chem. Rev.* **1999**, *185–186*, 471.
- (58) Taylor, C. P. S. *Biochim. Biophys. Acta* **1977**, 137.
- (59) Lang, G.; Marshall, W. *Proc. Phys. Soc.* **1966**, *87*, 3.
- (60) E_f^0 was calculated from the average of the oxidation and reduction peak potentials, using the assumption that diffusion coefficient of oxidized and reduced forms are equal.
- (61) The free ligand in CH_3CN (0.1 M $[\text{Bu}_4\text{N}](\text{PF}_6)$) exhibits an irreversible reduction process at very negative potential at $E_p^{\text{red}} = -1.78$ V, followed by two irreversible oxidation processes at $E_p^{\text{ox}} = -0.535$ and 1.15 V vs $[\text{FeCp}_2]^{0/+}$.
- (62) Muresan, N.; Chlopek, K.; Weyhermüller, T.; Neese, F.; Wieghardt, K. *Inorg. Chem.* **2007**, *46*, 5327.
- (63) Bruin, B. D.; Bill, E.; Bothe, E.; Weyhermüller, T.; Wieghardt, K. *Inorg. Chem.* **2000**, *39*, 2936.
- (64) (a) Mayoh, B.; Day, P. *J. Chem. Soc., Dalton Trans.* **1976**, 1483.
(b) Mayoh, B.; Day, P. *J. Chem. Soc., Dalton Trans.* **1974**, 896.
- (65) Rogez, G.; Marvilliers, A.; Rivière, E.; Audière, J.-P.; Lloret, F.; Varret, F.; Goujon, A.; Mendenez, N.; Girerd, J.-J.; Mallah, T. *Angew. Chem., Int. Ed.* **2000**, *39*, 2885.
- (66) Mochizuki, T.; Nogami, T.; Ishida, T. *Inorg. Chem.* **2009**, *48*, 2254.
- (67) Bachler, V.; Olbrich, V.; Neese, F.; Wieghardt, K. *Inorg. Chem.* **2002**, *41*, 4179.
- (68) Herebian, D.; Wieghardt, K.; Neese, F. *J. Am. Chem. Soc.* **2003**, *125*, 10997.